Supplementary Information for "Out-of-Plane Oscillating Electric Fields Unlock Low-Temperature Nonequilibrium Superionicity in Quasi-Two-Dimensional $AgCrSe_2$"

Jia-Wen Li,[1,2] Kun Yang,[1,2] Sheng Meng,[3,2,4] Xinghua Shi,[1,2] Wei-Hai Fang,[5] and Jin Zhang[1,2,*]

[1] *Laboratory of Theoretical and Computational Nanoscience, National Center for Nanoscience and Technology, Chinese Academy of Sciences, Beijing 100190, China*
[2] *University of Chinese Academy of Sciences, Beijing 100049, China*
[3] *Beijing National Laboratory for Condensed Matter Physics, and Institute of Physics, Chinese Academy of Sciences, Beijing 100190, China*
[4] *Songshan Lake Materials Laboratory, Dongguan, Guangdong 523808, China*
[5] *College of Chemistry, Key Laboratory of Theoretical and Computational Photochemistry of Ministry of Education, Beijing Normal University, Beijing 100875, China*

CONTENTS

Supplementary Note 1. Methods 2
1.1. Density functional theory calculations and construction of datasets 2
1.2. Machine-learning molecular dynamics simulations 2
Supplementary Note 2. Model parameters and performance for $AgCrSe_2$ 3
Supplementary Note 3. Temperature-dependent order parameter of Ag^+ ions 5
Supplementary Note 4. In-plane ionic conductivity 7
4.1. Static-field drift and conductivity 7
4.2. Field-resolved conductivities and high-temperature activation energy 7
Supplementary Note 5. Self-diffusion and conductivity-derived diffusion coefficients 11
Supplementary Note 6. Ionic transport under oscillating electric fields 13
Supplementary Note 7. Residence fractions under oscillating electric fields 17
Supplementary Note 8. Out-of-plane oscillating field-driven sublattice switching 19
8.1. Trajectory-resolved switching probabilities 19
8.2. Estimation of the characteristic switching timescale 24

Supplementary References 24

* jinzhang@nanoctr.cn

Supplementary Note 1. Methods

1.1. Density functional theory calculations and construction of datasets

All density-functional-theory (DFT) calculations were performed using the Vienna *Ab initio* Simulation Package (VASP) [1]. The electron–ion interactions were described using the projector-augmented-wave method [2], and exchange-correlation effects were treated within the Perdew–Burke–Ernzerhof (PBE) generalized-gradient approximation [3]. The plane-wave cutoff energy was set to 600 eV. The electronic self-consistency threshold was 10^{-5} eV. The Born effective charge (BEC) tensors were calculated using density-functional perturbation theory (DFPT) [4]. Spin-polarized calculations were performed, and the DFT-D3 dispersion correction was included in the energy and force calculations [5]. All DFT calculations were performed assuming ferromagnetic ordering.

For superionic $AgCrSe_2$, 120 1-ps first-principles canonical (NVT) trajectories were generated at 500, 550, 600, and 650 K (30 trajectories at each temperature) using 48-atom supercells, a 2 fs time step, under the Nosé thermostat [6]. Forty-one configurations were extracted from each trajectory, yielding 4920 structures. Additional low-temperature ordered configurations were extracted from 2-ps trajectories at 300 and 400 K. For each configuration, energies and forces were calculated using a Γ-centered $3 \times 3 \times 1$ k-point mesh, while BEC tensors were calculated for the configurations selected for the BEC dataset. After convergence and magnetic-state screening, 4384 structures were retained for the energy–force dataset. For the BEC dataset, additional screening excluded configurations with a density of states at the Fermi level exceeding 3 states eV^{-1} $cell^{-1}$, leaving 1058 structures.

To preserve the model accuracy in describing the disordered superionic phase, the high-temperature trajectories were divided into training, validation, and test sets in an approximately 70:15:15 ratio, with no trajectory shared among the three subsets. The additional 300 and 400 K configurations were partitioned separately within each temperature. The resulting energy–force dataset contained 3064, 667, and 653 structures in the training, validation, and test subsets, respectively; the corresponding BEC subsets contained 753, 164, and 141 structures.

1.2. Machine-learning molecular dynamics simulations

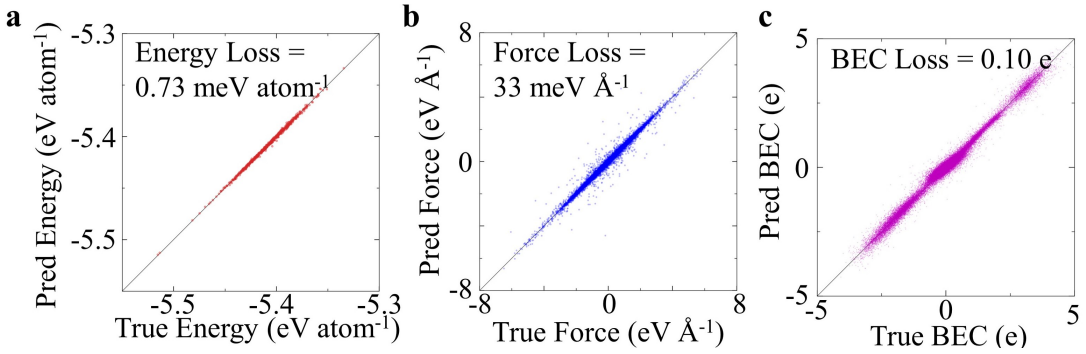
Machine-learning molecular dynamics (MLMD) simulations were performed using a $3 \times 3 \times 1$ supercell constructed from the 48-atom orthorhombic DFT cell, containing 432 atoms (108 Cr, 108 Ag, and 216 Se atoms). The equations of motion were integrated with a 1 fs time step using the Atomic Simulation Environment [7]. Temperature was controlled using a Langevin thermostat with a damping time of approximately 0.34 ps.

Supplementary Note 2. Model parameters and performance for $AgCrSe_2$

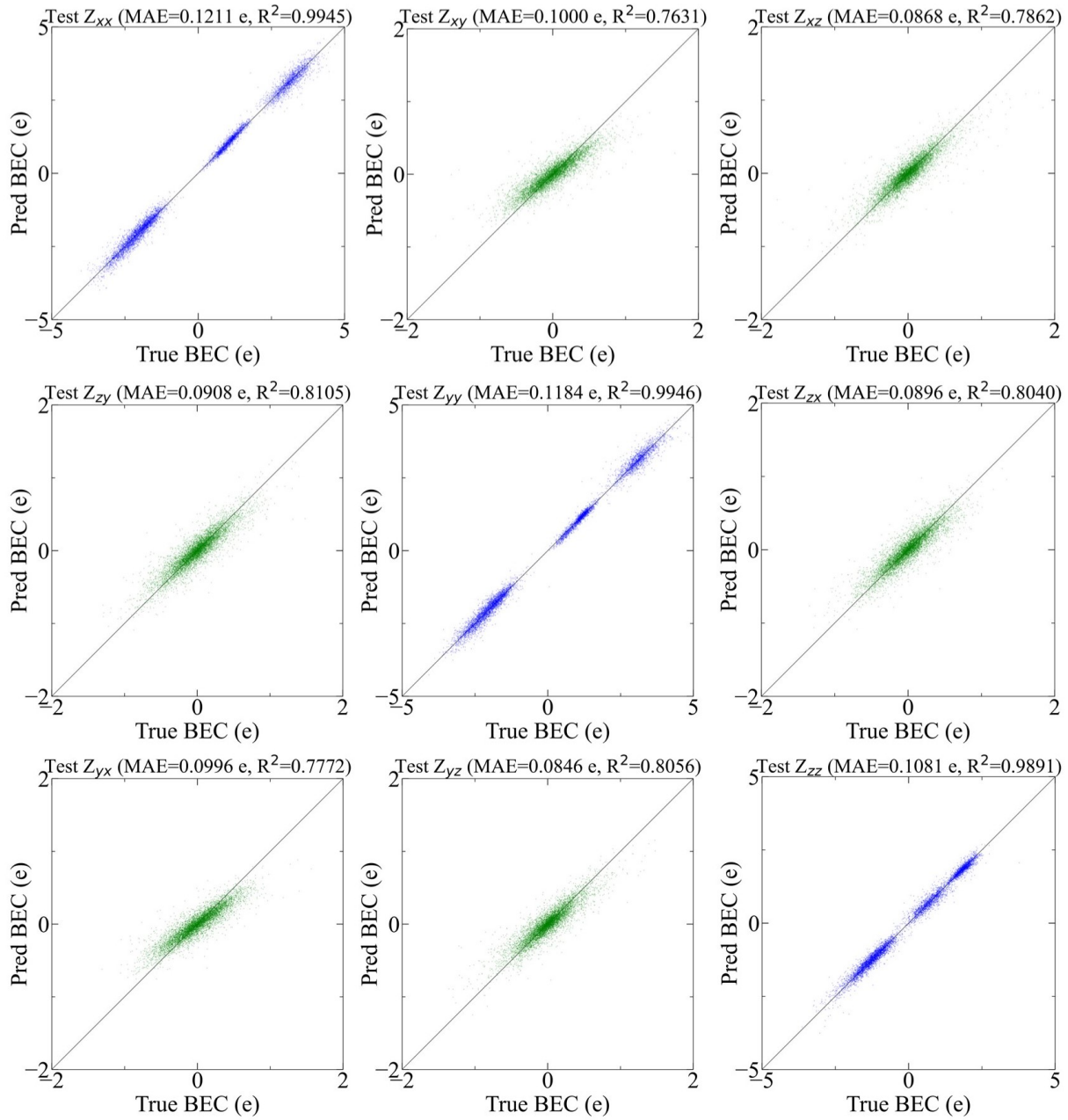
Two complementary parameter-separated branches of EFR-GNN [8] were employed for $AgCrSe_2$: an energy–force branch and a BEC branch. The cutoff radius was set to $r_{\mathrm{cut}} = 7.0$ Å, the radial dependence was expanded using 20 Bessel basis functions, and the spherical-harmonic representation was set to $\mathrm{irreps}_{\mathrm{sh}} = 1\times0e+1\times1o+1\times2e$. The BEC branch consisted of four message-passing blocks without edge updates, with $84\times0e+8\times1o+6\times1e+4\times2e+3\times2o$ used as the hidden irreps for both node and edge features. The energy–force branch consisted of two message-passing blocks without edge updates, with $64\times0e+6\times1o+4\times2e$ used for both node and edge features.

Atom-resolved loss terms were normalized using element-specific standard deviations determined from the training set, while tensorial quantities were additionally normalized by Cartesian component. Training was performed using the Adam optimizer with a batch size of 64 structures and an initial learning rate of 5×10^{-3}. The loss function was based on normalized mean absolute errors (MAEs), with relative weights of 1:100 for energy and force and equal weights for the nine BEC components. Atomic forces were obtained as the negative gradient of the predicted total energy, and the predicted BEC tensors were constrained to satisfy the acoustic sum rule (ASR).

The trained EFR-GNN models showed good agreement with the DFT reference values for energies, atomic forces, and BEC tensors of $AgCrSe_2$. The test-set MAEs were 0.73 meV atom^{-1} for energy, 33 meV Å^{-1} for atomic forces, and approximately 0.10e for BEC tensor components (Supplementary Figure 1). All nine Cartesian components of the BEC tensors were further benchmarked against the DFPT reference values in Supplementary Fig. 2, with component-wise MAEs ranging from approximately 0.085e to 0.121e.



Supplementary Figure 1. **Performance of EFR-GNN on the $AgCrSe_2$ test set.** Comparison between reference and predicted values for (**a**) energy per atom, (**b**) atomic-force components, and (**c**) BEC tensor components. The corresponding mean absolute errors (MAEs) are 0.73 meV atom^{-1}, 33 meV Å^{-1}, and approximately 0.10e.



Supplementary Figure 2. **Component-wise performance of the BEC model on the $AgCrSe_2$ test set.** Comparison between DFPT reference values and EFR-GNN predictions for the nine Cartesian components of the BEC tensor. The MAE and coefficient of determination R^2 are indicated in each panel.

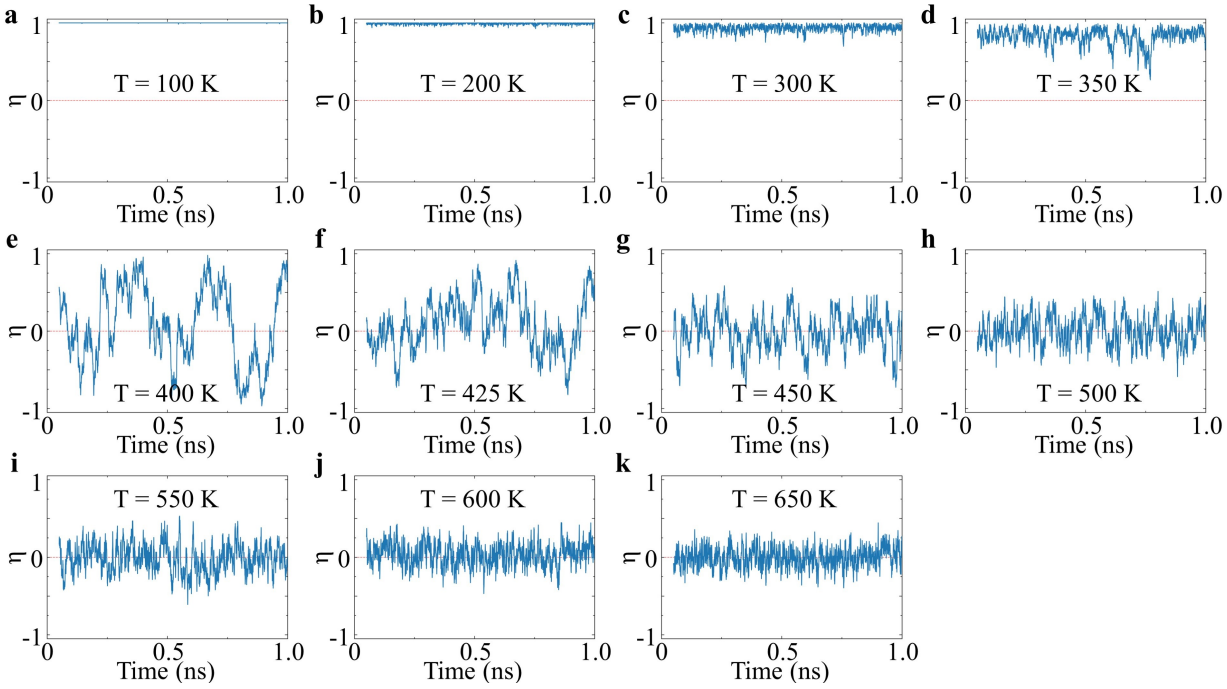
Supplementary Note 3. Temperature-dependent order parameter of Ag^+ ions

The Ag^+ ions were assigned to the two symmetry-equivalent α and β sublattices according to their proximity to the corresponding reference sites. The instantaneous sublattice order parameter was defined as

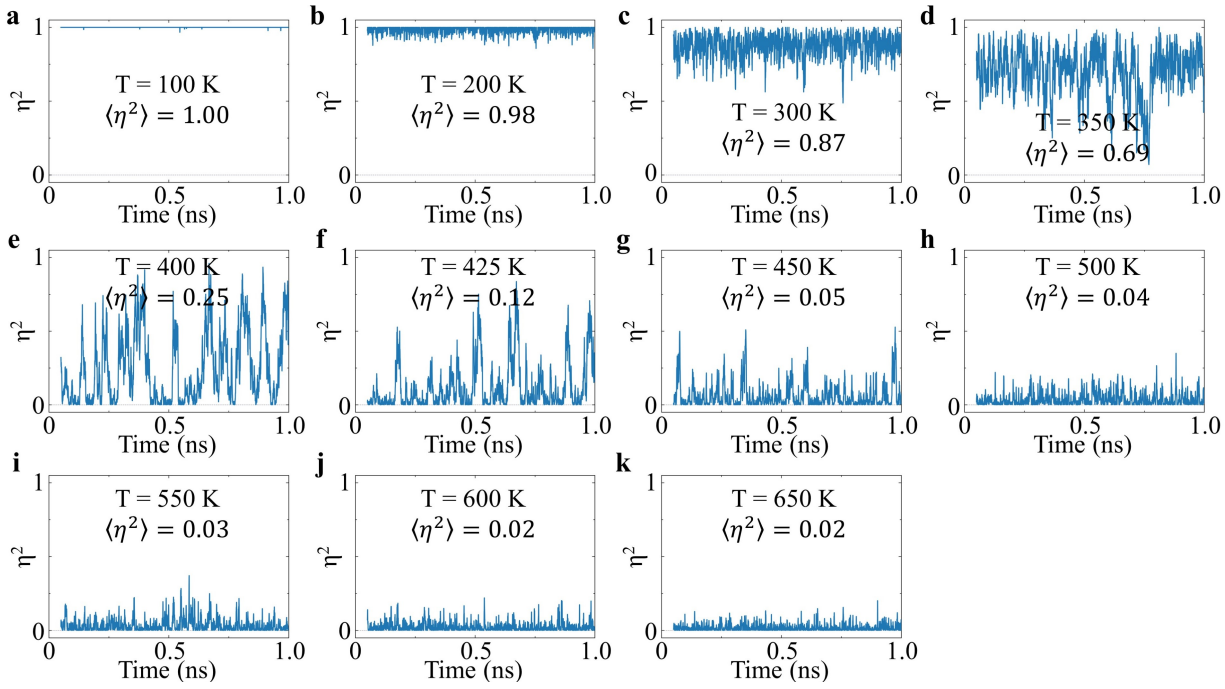
$$\eta(t) = \frac{N_\alpha(t) - N_\beta(t)}{N_{\text{tot}}}, \qquad N_\alpha(t) + N_\beta(t) = N_{\text{tot}}, \tag{S1}$$

where N_α and N_β are the instantaneous numbers of Ag^+ ions occupying the α and β sublattices, respectively, and $N_{\text{tot}} = 108$. Accordingly, $|\eta| \simeq 1$ represents an ordered state dominated by one sublattice, whereas $\eta \simeq 0$ corresponds to nearly equal occupation of the two sublattices. To characterize the degree of sublattice ordering independent of its polarity, we use the time-averaged squared order parameter $\langle\eta^2\rangle$.

Supplementary Figs. 3 and 4 show the temperature evolution of the Ag-sublattice order in the absence of an external field. At 100 and 200 K, the Ag^+ sublattice remains almost fully ordered, with $\langle\eta^2\rangle = 1.00$ and 0.98, respectively. With increasing temperature, $\langle\eta^2\rangle$ decreases to 0.87 at 300 K and 0.69 at 350 K, followed by a rapid reduction to 0.25 at 400 K, 0.12 at 425 K, and 0.05 at 450 K. At still higher temperatures, $\langle\eta^2\rangle$ remains close to zero, with values of 0.04, 0.03, 0.02, and 0.02 at 500, 550, 600, and 650 K, respectively. These results indicate a progressive loss of Ag-sublattice order with increasing temperature, with the dynamically disordered superionic state essentially established by approximately 450 K.



Supplementary Figure 3. **Temperature-dependent Ag-sublattice order.** Time evolution of the Ag-sublattice order parameter η in zero field at (**a**) 100, (**b**) 200, (**c**) 300, (**d**) 350, (**e**) 400, (**f**) 425, (**g**) 450, (**h**) 500, (**i**) 550, (**j**) 600, and (**k**) 650 K.



Supplementary Figure 4. **Temperature dependence of the squared order parameter.** Squared order parameter η^2 for the zero-field trajectories in Supplementary Fig. 3. The panel-to-temperature correspondence is the same as in Supplementary Fig. 3, and the time-averaged $\langle\eta^2\rangle$ is indicated in each panel.

Supplementary Note 4. In-plane ionic conductivity

4.1. Static-field drift and conductivity

To evaluate the in-plane ionic transport, static electric fields E_x were applied at different temperatures, and the in-plane motion of Ag^+ ions was calculated with periodic boundary conditions taken into account. The resulting ensemble-averaged Ag^+ displacements are shown in Supplementary Figs. 6 and 5. The drift velocity v_x was obtained from a linear fit to the displacement after 50 ps. For 350–650 K, fields of $E_x = \pm 0.001$ and ± 0.0025 V Å^{-1} were used, whereas $E_x = \pm 0.005$ V Å^{-1} was used at 300 K because the drift under weaker fields was too small.

The field-dependent drift velocities are shown in Supplementary Fig. 7 and were fitted using

$$v_x = k_E E_x, \qquad k_E = \frac{\sum_{j=1}^{N_E} E_{x,j} v_{x,j}}{\sum_{j=1}^{N_E} E_{x,j}^2}, \tag{S2}$$

where k_E gives the Ag^+ mobility along the x direction. The corresponding ionic conductivity was then calculated as

$$\mu_x = k_E, \qquad \sigma_x = n_{\mathrm{Ag}} e \mu_x, \qquad n_{\mathrm{Ag}} = \frac{N_{\mathrm{tot}}}{V}, \tag{S3}$$

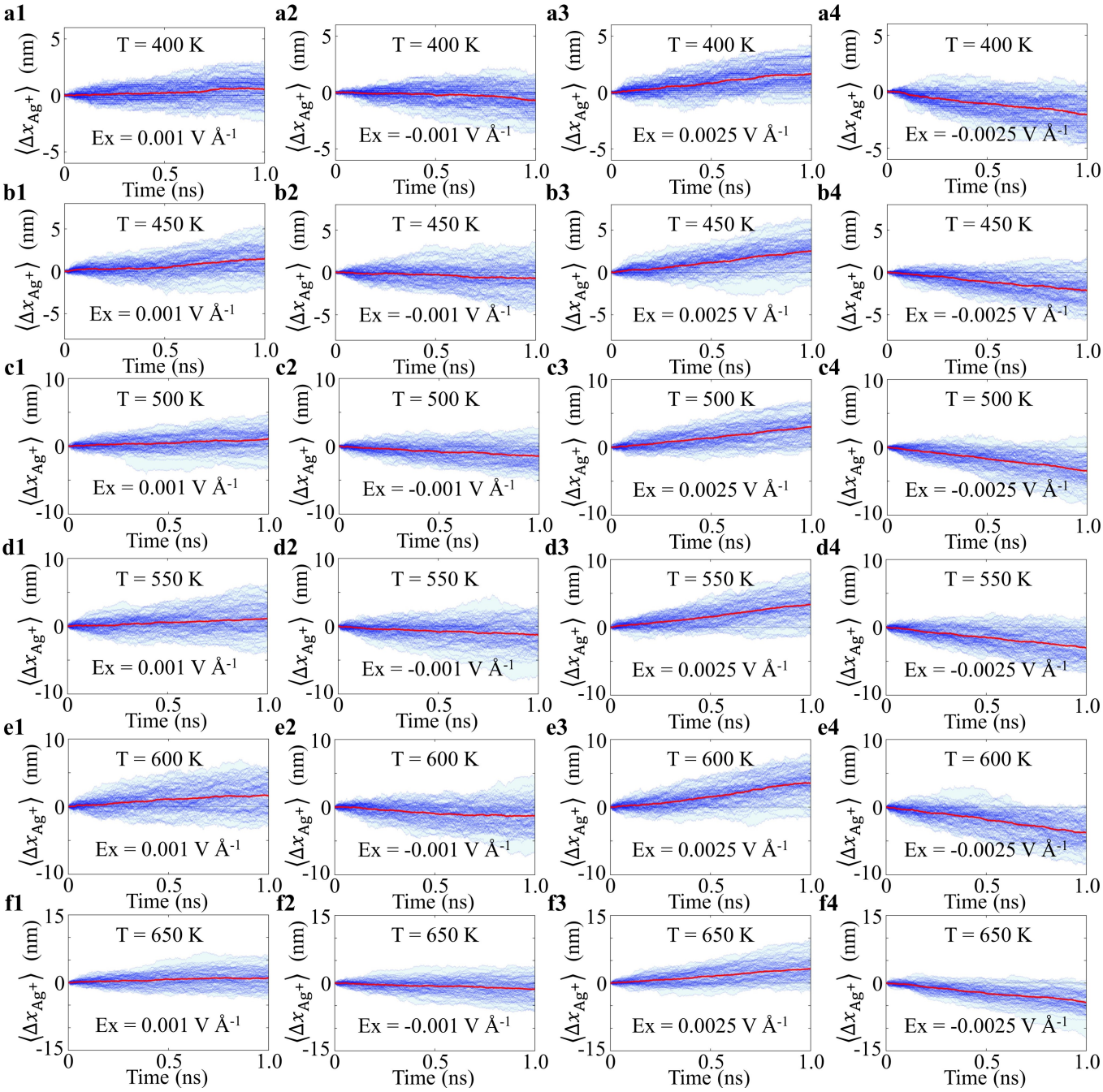
where $n_{\mathrm{Ag}} = 1.165 \times 10^{22}$ cm^{-3} is the Ag number density. The nominal ionic charge $+e$ was used to convert the Ag^+ drift into ionic current, while the Born effective charges were used only to describe the coupling between the electric field and the lattice. The resulting ionic conductivities are summarized in Supplementary Table 1.

Supplementary Table 1. Ionic conductivities obtained from the static-field drift velocities using Eq. (S3).

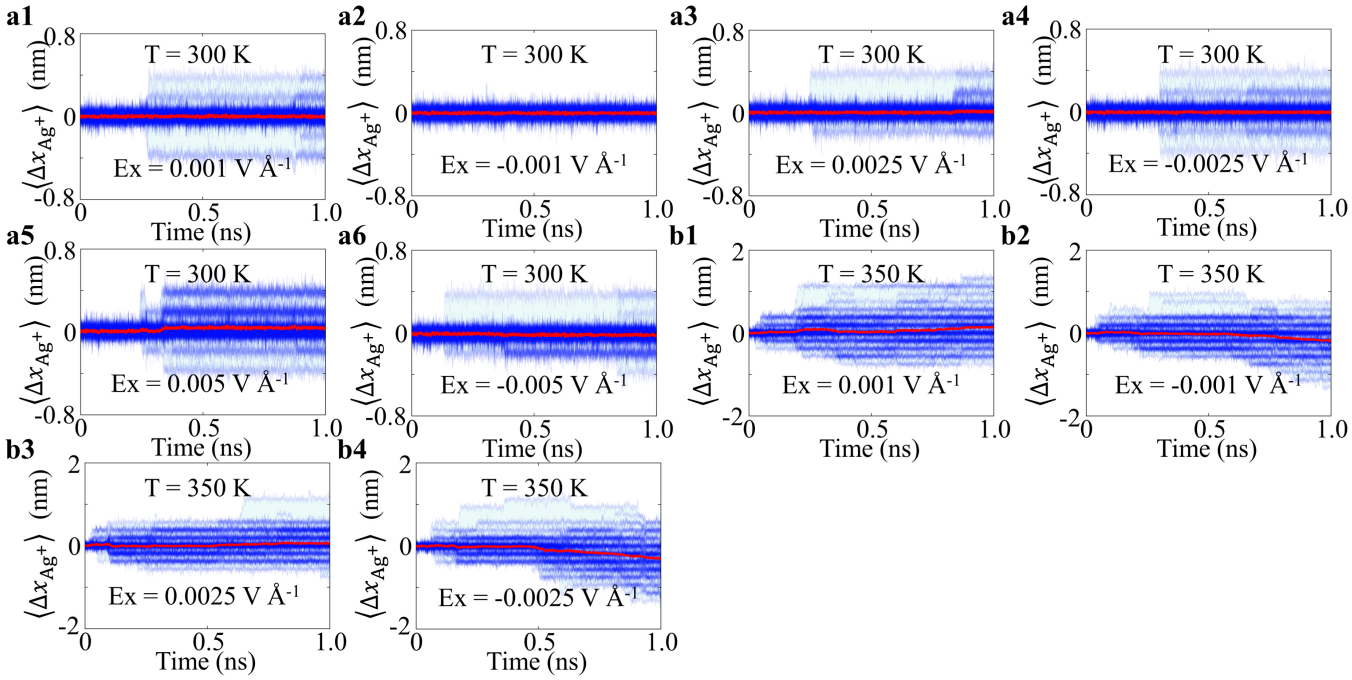
T (K)	σ_x (S cm^{-1})	Fields considered (V Å^{-1})
300	0.011	± 0.005
350	0.173	± 0.001, ± 0.0025
400	1.345	± 0.001, ± 0.0025
450	1.837	± 0.001, ± 0.0025
500	2.395	± 0.001, ± 0.0025
550	2.362	± 0.001, ± 0.0025
600	2.954	± 0.001, ± 0.0025
650	2.690	± 0.001, ± 0.0025

4.2. Field-resolved conductivities and high-temperature activation energy

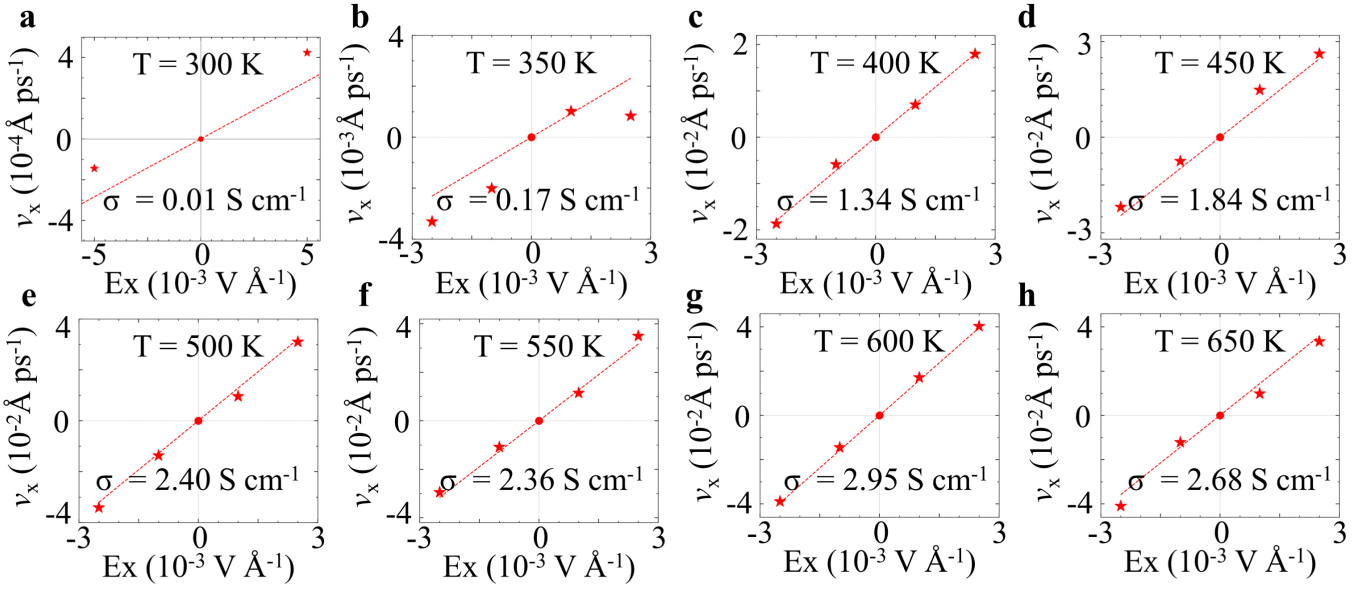
The conductivity estimates for each temperature and applied electric field are given in the captions of Supplementary Figs. 6 and 5. For each field, the conductivity was evaluated as $\sigma_x = n_{\mathrm{Ag}} e v_x / E_x$, using the drift velocity obtained from the displacement fit after 50 ps. At 300 K, all six field-dependent estimates are provided, while only the $E_x = \pm 0.005$ V Å^{-1} points were used in the joint drift fit reported in Supplementary Table 1. The negative estimates at weaker fields reflect unresolved drift within the finite trajectories rather than a negative physical conductivity. The high-temperature fit uses the five temperatures from 450 to 650 K and the form $\sigma T = A_\sigma \exp[-E_a/(k_B T)]$, where A_σ is the fitted prefactor and E_a is the activation energy. The linear fit of $\ln(\sigma T)$ against $1000/T$ gives $E_a = 97.2$ meV and $R^2 = 0.942$.



Supplementary Figure 5. **Ag drift under static electric fields at 400–650 K.** Ag displacements under static in-plane electric fields at 400–650 K. Rows **a**–**f** correspond to 400, 450, 500, 550, 600, and 650 K, respectively. Columns **1**–**4** correspond to $E_x = +0.001$, -0.001, $+0.0025$, and -0.0025 V Å^{-1}. In column order **1**–**4**, the conductivity estimates σ_x (S cm^{-1}) are (**a**) 1.310, 1.098, 1.341, 1.394; (**b**) 2.765, 1.405, 1.955, 1.639; (**c**) 1.781, 2.559, 2.314, 2.549; (**d**) 2.141, 2.031, 2.609, 2.204; (**e**) 3.192, 2.699, 3.009, 2.902; (**f**) 2.043, 2.267, 2.493, 3.059. Thin blue curves show individual Ag ions, and red curves show their mean displacement.



Supplementary Figure 6. **Low-temperature Ag drift under static electric fields.** Ag displacements under static in-plane electric fields at (**a1**–**a6**) 300 K and (**b1**–**b4**) 350 K. Panels **a1**–**a6** correspond to E_x = +0.001, −0.001, +0.0025, −0.0025, +0.005, and −0.005 V Å^{-1}; panels **b1**–**b4** correspond to the first four fields. The corresponding conductivity estimates σ_x (S cm^{-1}) are −0.001, 0.001, 0.007, -1.270×10^{-4}, 0.016, 0.005 for panels **a1**–**a6**, respectively, and 0.191, 0.375, 0.062, 0.247 for panels **b1**–**b4**, respectively. Thin blue curves show individual Ag ions, and red curves show their mean displacement.



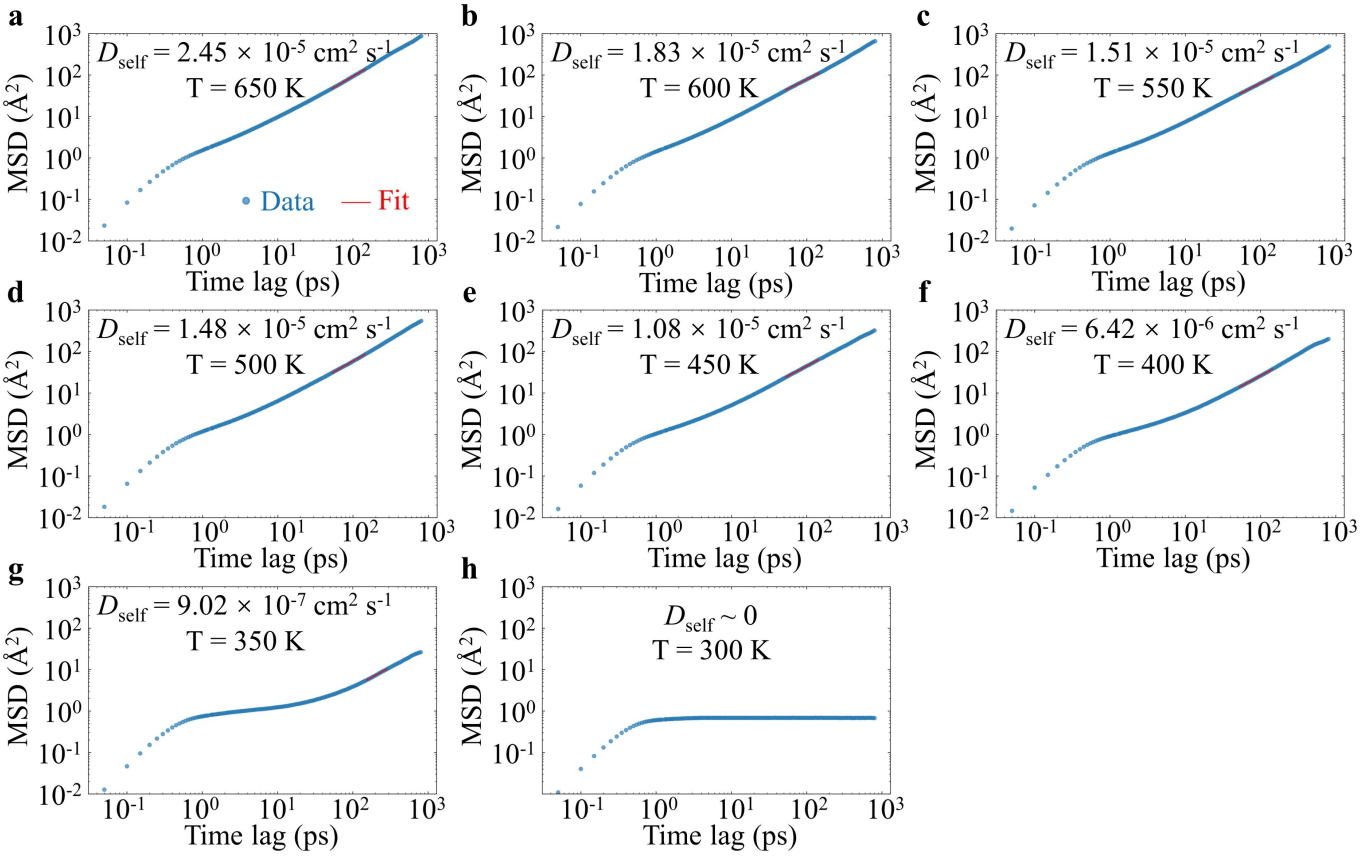
Supplementary Figure 7. **Field-dependent Ag drift velocities and ionic conductivities at different temperatures.** Ag drift velocity as a function of the static in-plane electric field at (**a**) 300, (**b**) 350, (**c**) 400, (**d**) 450, (**e**) 500, (**f**) 550, (**g**) 600, and (**h**) 650 K. Red stars are velocities obtained from the displacement trajectories, and dashed lines are linear fits constrained to pass through the origin. The fitted conductivities are indicated in the panels. Panel **a** uses $E_x = \pm 0.005$ V Å^{-1} to resolve the weak Ag^+ drift at 300 K, whereas panels **b**–**h** use $E_x = \pm 0.001$ and ± 0.0025 V Å^{-1}.

Supplementary Note 5. Self-diffusion and conductivity-derived diffusion coefficients

The in-plane Ag^+ self-diffusion coefficient was calculated from 1-ns zero-field MLMD trajectories using the same supercell and thermostat settings described above. Periodic boundary crossings were unwrapped, and the Ag displacements were referenced to the mean displacement of the Cr–Se framework. The in-plane mean-square displacement (MSD) was evaluated as

$$\mathrm{MSD}_{ab}(\tau) = \frac{1}{N_{\mathrm{tot}}} \sum_{i=1}^{N_{\mathrm{tot}}} \left\langle |\mathbf{r}_{i,ab}(t_0+\tau) - \mathbf{r}_{i,ab}(t_0)|^2 \right\rangle_{t_0}, \tag{S4}$$

where $\mathbf{r}_{i,ab}$ is the unwrapped, framework-referenced in-plane position of Ag ion i, $N_{\mathrm{tot}} = 108$ is the number of Ag ions, τ is the time lag, and $\langle \cdots \rangle_{t_0}$ denotes averaging over all available time origins t_0. The diffusion coefficient was obtained from a linear fit, $\mathrm{MSD}_{ab}(\tau) = a\tau + b$, using $D_{\mathrm{self}} = a/4$, where a and b are the fitted slope and intercept, respectively, and the factor of four corresponds to two-dimensional diffusion. The fitting intervals were 50–150 ps at 400–650 K and 150–300 ps at 350 K. The MSD curves and fits are shown in Supplementary Fig. 8. At 300 K, the MSD reaches a plateau and normal diffusion is not resolved within the simulated time.



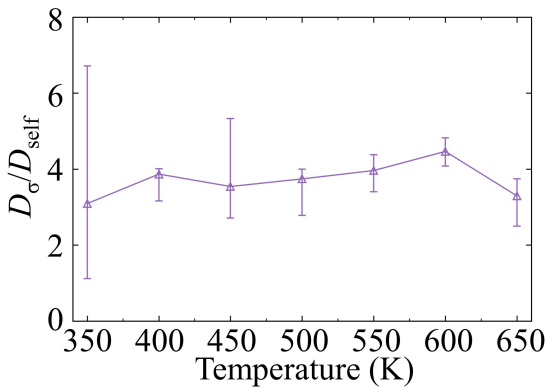
Supplementary Figure 8. **Zero-field Ag self-diffusion.** In-plane Ag^+ MSDs from zero-field MLMD simulations at (**a**) 650, (**b**) 600, (**c**) 550, (**d**) 500, (**e**) 450, (**f**) 400, (**g**) 350, and (**h**) 300 K. Blue points show the MSDs, and red lines show the linear fits used to determine D_{self}. The fitting intervals are 50–150 ps for panels **a**–**f** and 150–300 ps for panel **g**. The plateau in panel **h** indicates that normal diffusion is not resolved at 300 K over the simulated time.

To compare single-ion diffusion with collective transport, a conductivity-derived diffusion coefficient was obtained from the static-field conductivity in Eq. (S3):

$$D_\sigma = \frac{k_{\mathrm{B}} T \sigma_x}{n_{\mathrm{Ag}} e^2} = \frac{k_{\mathrm{B}} T \mu_x}{e}, \qquad f_{\mathrm{NE}} = \frac{D_\sigma}{D_{\mathrm{self}}}, \tag{S5}$$

where k_{B} is the Boltzmann constant, T is the absolute temperature, and e is the elementary charge; σ_x, μ_x, and n_{Ag} are defined above. Here, D_σ is obtained from the in-plane drift response, whereas D_{self} is independently determined

from zero-field single-ion diffusion. For 350–650 K, where normal diffusion is resolved, the resulting f_{NE} values range from approximately 3.1 to 4.5, as shown in Supplementary Fig. 9. This several-fold enhancement of charge transport relative to self-diffusion is comparable to the Nernst–Einstein factor of approximately three reported above 325 K [9] and is compatible with correlated Ag^+ motion. Such correlations have also been associated with short-range Ag^+ dimers and trimers during fast diffusion [10].



Supplementary Figure 9. **Conductivity-derived versus self-diffusion.** Ratio $D_\sigma/D_{\mathrm{self}}$ at 350–650 K, where D_σ is obtained from the static-field drift response and D_{self} from zero-field Ag^+ self-diffusion. Central values correspond to the fitted static-field conductivities, while error bars indicate the range obtained from the individual applied fields.

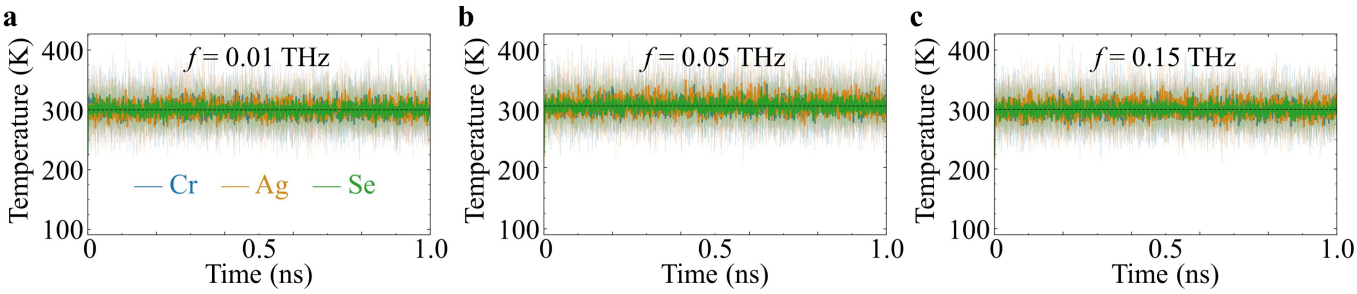
Supplementary Note 6. Ionic transport under oscillating electric fields

In-plane ionic transport was probed using a constant field E_x. For the 300 K frequency-dependent series, a constant probe field $E_x = +0.0025$ V Å^{-1} was applied together with an oscillating out-of-plane field

$$E_z(t) = \begin{cases} E_z^0 \sin[2\pi f(t - t_\phi)], & 100 \le t \le 900 \text{ ps}, \\ 0, & \text{otherwise}, \end{cases} \tag{S6}$$

with amplitude $E_z^0 = 0.030$ V Å^{-1}, frequency f in THz, time t in ps, and phase-reference time $t_\phi = 20$ ps. The driving frequency was varied from 0.005 to 0.200 THz.

To assess whether the enhanced ionic transport is accompanied by sustained heating, the species-resolved kinetic temperatures were examined for representative trajectories at 0.01, 0.05, and 0.15 THz. As shown in Supplementary Fig. 10, the temperatures of Cr, Ag, and Se remain centered around 300 K without a sustained increase. This behavior indicates that the enhanced transport is not associated with persistent field-induced heating.



Supplementary Figure 10. **Species-resolved temperatures under oscillating electric fields.** Temperatures of Cr, Ag, and Se at 300 K for (**a**) 0.01, (**b**) 0.05, and (**c**) 0.15 THz. Thick lines show moving averages with a 1 ps window, and thin lines show the raw temperature traces. The oscillating field has amplitude $E_z^0 = 0.030$ V Å^{-1} and is applied from 100 to 900 ps, together with a constant in-plane probe field $E_x = +0.0025$ V Å^{-1}. All species remain centered around 300 K without sustained heating.

For the field-driven trajectories in Supplementary Figs. 11 and 12, the ionic conductivity was determined from the net Ag drift over the common field-on interval,

$$v_x^{\text{on}} = \frac{\overline{\Delta x}(t_b) - \overline{\Delta x}(t_a)}{t_b - t_a}, \qquad \sigma_x^{\text{on}} = n_{\text{Ag}} e \frac{v_x^{\text{on}}}{E_x}, \tag{S7}$$

where $t_a = 100$ ps, $t_b = 900$ ps, and $E_x = +0.0025$ V Å^{-1}. The resulting conductivities are approximately 0.89, 1.73, and 0.24 S cm^{-1} at 0.01, 0.05, and 0.15 THz, respectively, capturing the pronounced frequency dependence of the field-driven ionic transport.

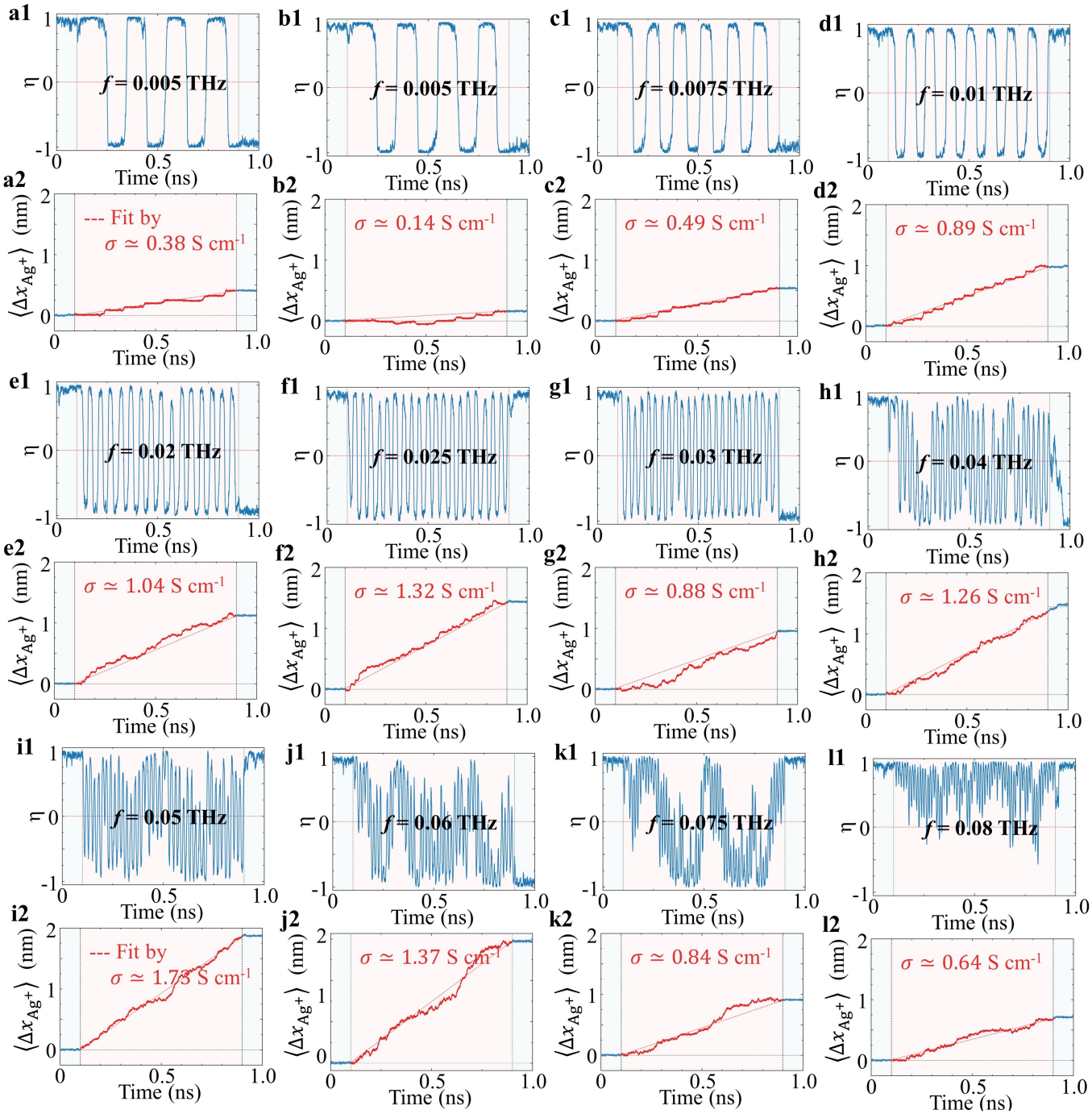
The field-induced dynamic disorder of the Ag sublattice was characterized by the central-region residence fraction

$$P_{0.3} = \frac{1}{M_{\text{on}}} \sum_{m=1}^{M_{\text{on}}} \mathbf{1}[|\eta(t_m)| < 0.3], \tag{S8}$$

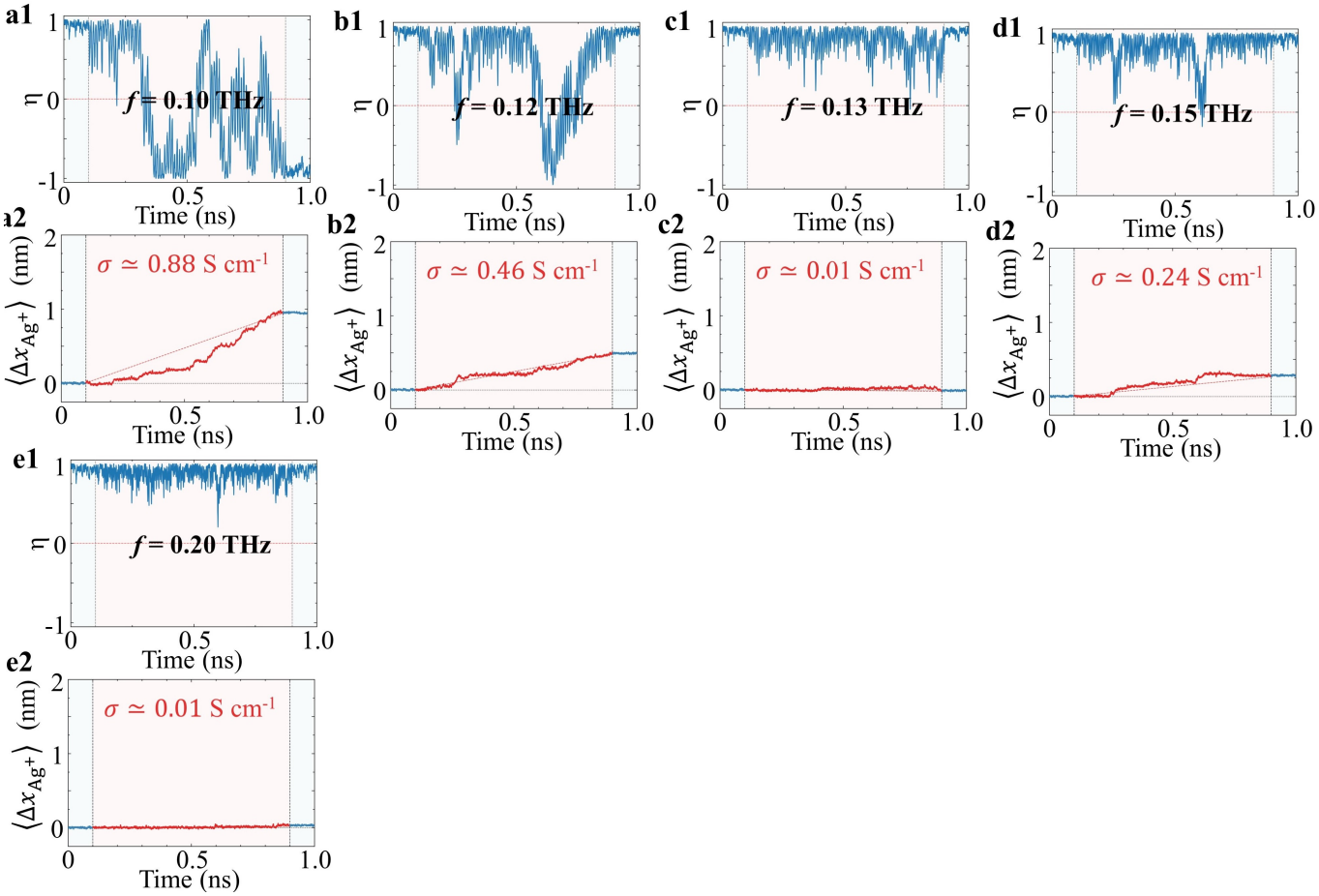
where M_{on} is the number of sampled configurations within the field-on interval and $\mathbf{1}[\cdot]$ equals one when the specified condition is satisfied and zero otherwise. $P_{0.3}$ therefore represents the fraction of time for which the Ag sublattice remains near balanced α/β occupation. Using the same 100–900 ps interval as the transport analysis, $P_{0.3} = 0.10$ was taken as an operational threshold for sustained access to the dynamically disordered regime. The corresponding frequency dependence of $P_{0.3}$ and the ionic conductivity σ at 300 K is summarized in Supplementary Table 2, with σ obtained from the fitted mean Ag drift over the same interval through $\sigma = n_{\text{Ag}} e v_x / E_x$.

Supplementary Table 2. Central-region residence fraction $P_{0.3}$ and in-plane ionic conductivity σ at 300 K under an oscillating out-of-plane field with $E_z^0 = 0.030$ V Å^{-1} and a constant in-plane probe field $E_x = +0.0025$ V Å^{-1}. Both quantities are evaluated over 100–900 ps. The tabulated conductivities are obtained from linear fits to the mean Ag displacement, whereas the values annotated in Supplementary Figs. 11 and 12 are determined from the net displacement over the same interval using Eq. (S7). The two entries at 0.005 THz represent independent trajectories.

f (THz)	$P_{0.3}$	σ (S cm^{-1})
0.005[a]	0.029	0.371
0.005[b]	0.030	0.136
0.0075	0.035	0.537
0.010	0.054	0.983
0.020	0.086	1.066
0.025	0.107	1.314
0.030	0.133	0.915
0.040	0.183	1.333
0.050	0.243	1.697
0.060	0.259	1.462
0.075	0.219	1.027
0.080	0.128	0.669
0.100	0.196	0.946
0.120	0.143	0.427
0.130	0.018	0.040
0.150	0.035	0.328
0.200	0.001	0.022



Supplementary Figure 11. **Frequency-dependent Ag-sublattice dynamics and ionic transport.** Results at 300 K for $E_z^0 = 0.030$ V Å^{-1} and $E_x = +0.0025$ V Å^{-1}. For each frequency, panels **1** and **2** show $\eta(t)$ and the mean Ag displacement relative to the Cr–Se framework, respectively. The frequencies are (**a,b**) 0.005, (**c**) 0.0075, (**d**) 0.01, (**e**) 0.02, (**f**) 0.025, (**g**) 0.03, (**h**) 0.04, (**i**) 0.05, (**j**) 0.06, (**k**) 0.075, and (**l**) 0.08 THz. Pink shading marks the 100–900 ps field-on interval, and the straight lines connect the displacement endpoints used to determine the annotated conductivities.



Supplementary Figure 12. **Ag-sublattice dynamics and ionic transport at higher frequencies.** Results at (**a**) 0.10, (**b**) 0.12, (**c**) 0.13, (**d**) 0.15, and (**e**) 0.20 THz. All simulation conditions and panel definitions are the same as in Supplementary Fig. 11. The annotated conductivities are determined from the net Ag displacement over the 100–900 ps field-on interval.

Supplementary Note 7. Residence fractions under oscillating electric fields

Simulations at 250 and 300 K were performed without an in-plane probe field. For these field-only trajectories, the central-region residence fraction was evaluated over the available field-on interval as

$$P_{0.3} = \frac{1}{t_b - t_a} \int_{t_a}^{t_b} \mathbf{1}[|\eta(t)| < 0.3], dt, \tag{S9}$$

where t_a and t_b denote the beginning and end of the analyzed interval. Crossings of $\eta = \pm 0.3$ were located by linear interpolation between adjacent sampled frames. Here, $t_a = 20$ ps, and the available field-on intervals differ from the common 100–900 ps window used for the transport series. $P_{0.3}$ values were used for classification, with $P_{0.3} \geq 0.1$ adopted as an operational criterion for sustained dynamic disorder rather than a sharp boundary for ionic conductivity. The tabulated results show that the dynamically disordered regime extends to higher frequencies with increasing field amplitude or temperature. Repeated field–frequency conditions represent independent trajectories and are listed separately.

Supplementary Table 3. Central-region residence fractions at 250 K under oscillating out-of-plane electric fields, with $E_x = 0$.

E_z^0 (V Å^{-1})	f (THz)	$P_{0.3}$	E_z^0 (V Å^{-1})	f (THz)	$P_{0.3}$
0.025	0.015	0.106	0.075	0.100	0.173
	0.020	0.103		0.150	0.304
	0.025	0.106		0.200	0.344
	0.040	0.000		0.300	0.004
	0.050	0.008	0.100	0.100	0.133
	0.060	0.000		0.150	0.192
0.030	0.025	0.076		0.200	0.287
	0.050	0.076		0.300	0.367
	0.075	0.012		0.400	0.072
	0.100	0.000		0.500	0.001
0.050	0.050	0.129		0.600	0.000
	0.075	0.224		0.700	0.000
	0.100	0.262		0.800	0.000
	0.150	0.054		0.900	0.000
	0.200	0.000			
	0.250	0.000			
	0.300	0.000			

Supplementary Table 4. Central-region residence fractions at 300 K under oscillating out-of-plane electric fields, with $E_x = 0$.

E_z^0 (V Å^{-1})	f (THz)	$P_{0.3}$	E_z^0 (V Å^{-1})	f (THz)	$P_{0.3}$
0.025	0.025	0.144	0.075	0.050	0.087
	0.050	0.222		0.200	0.388
	0.075	0.084		0.300	0.238
	0.100	0.000		0.400	0.041
	0.500	0.000		0.500	0.000
	1.000	0.000		0.600	0.000
	5.000	0.000	0.100	0.050	0.085
0.030	0.030	0.127		0.075	0.103
	0.040	0.184		0.100	0.140
	0.050	0.184		0.150	0.194
	0.100	0.053		0.200	0.265
	0.200	0.000		0.300	0.445
	0.300	0.000		0.400	0.472
0.050	0.050	0.124		0.500	0.169
	0.100	0.278		0.600	0.051
	0.150	0.381		0.700	0.025
	0.200	0.020		0.800	0.000
	0.250	0.001		0.900	0.000
	0.300	0.000		1.000	0.000
	0.500	0.000		5.000	0.000
	1.000	0.000			
	5.000	0.000			

Supplementary Note 8. Out-of-plane oscillating field-driven sublattice switching

8.1. *Trajectory-resolved switching probabilities*

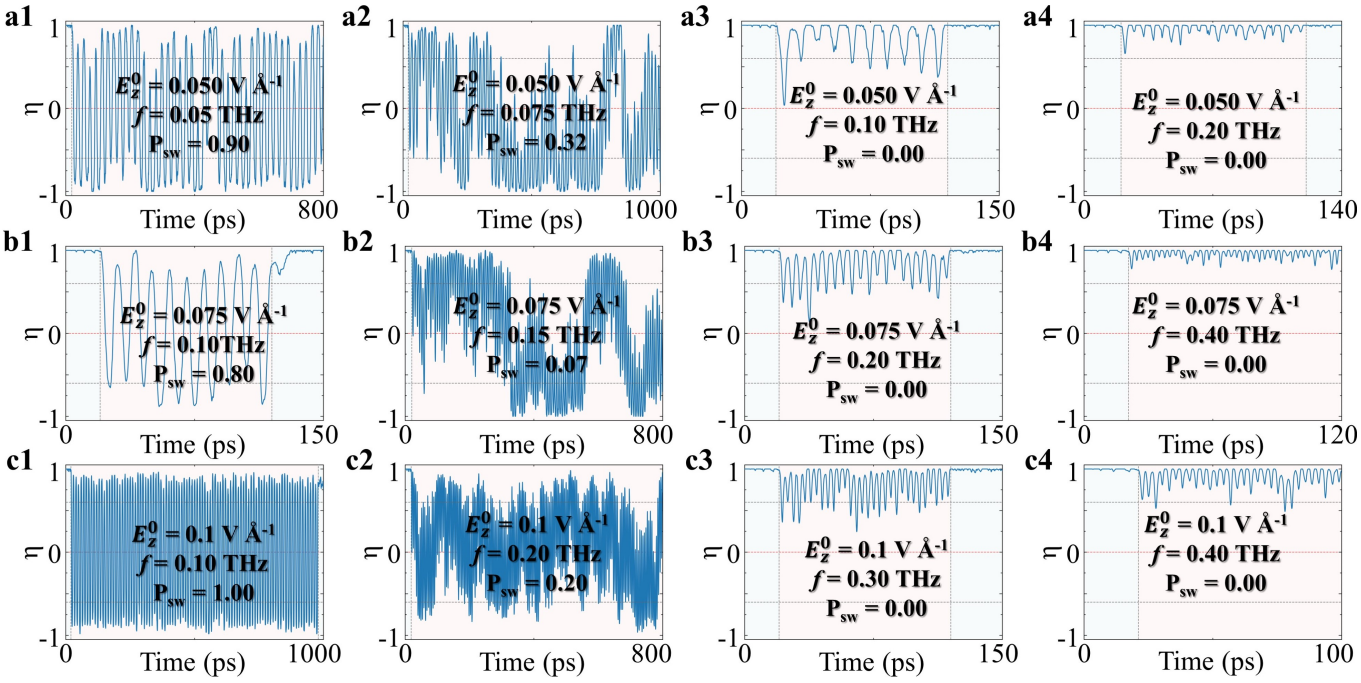
Field-driven Ag-sublattice switching was examined at 200, 250, and 300 K over a range of field amplitudes and frequencies, without an in-plane probe field. Representative trajectories are shown in Supplementary Figs. 13–15.

The switching probability was evaluated cycle by cycle over complete periods of the oscillating out-of-plane field. For the kth cycle C_k, a switching event was identified when the order parameter reached both $+\eta_c$ and $-\eta_c$, with $\eta_c = 0.6$:

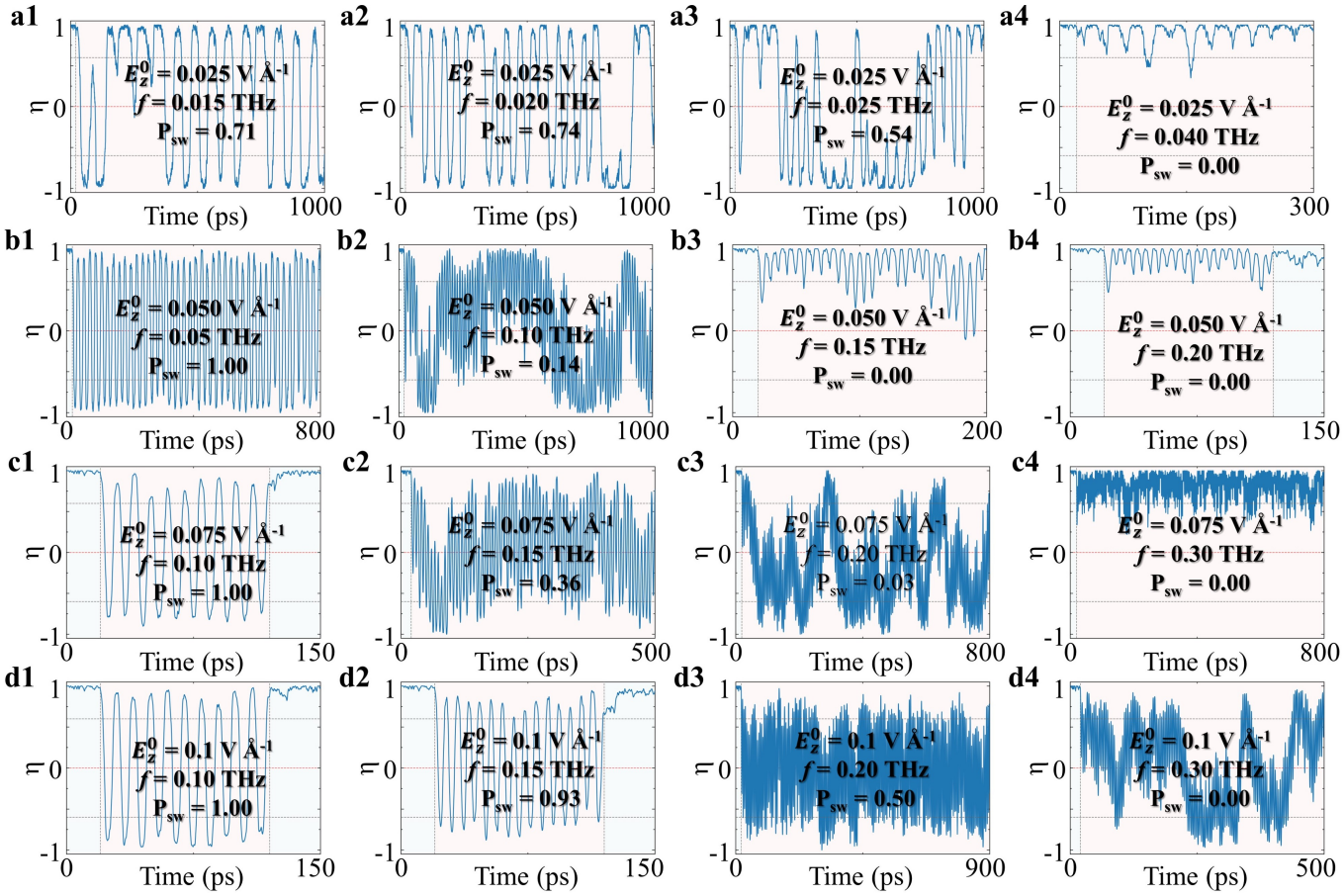
$$I_k = \mathbf{1}\left[\max_{t\in C_k}\eta(t) \geq \eta_c \text{ and } \min_{t\in C_k}\eta(t) \leq -\eta_c\right], \qquad P_{\mathrm{sw}} = \frac{1}{N_c}\sum_{k=1}^{N_c} I_k. \tag{S10}$$

Here, N_c is the number of complete field cycles within the analyzed interval, with cycle boundaries determined from the phase of the applied field and partial cycles at the interval boundaries excluded. All complete cycles, including the first, were evaluated using the unsmoothed order parameter. Once both thresholds were reached within a cycle, that cycle was counted as a switching event, without requiring a subsequent return to the initial sublattice within the same cycle. Accordingly, P_{sw} quantifies the fraction of field cycles in which the Ag sublattice traverses between the two ordered sides, whereas $P_{0.3}$ in Eq. (S8) measures the residence fraction near balanced sublattice occupation.

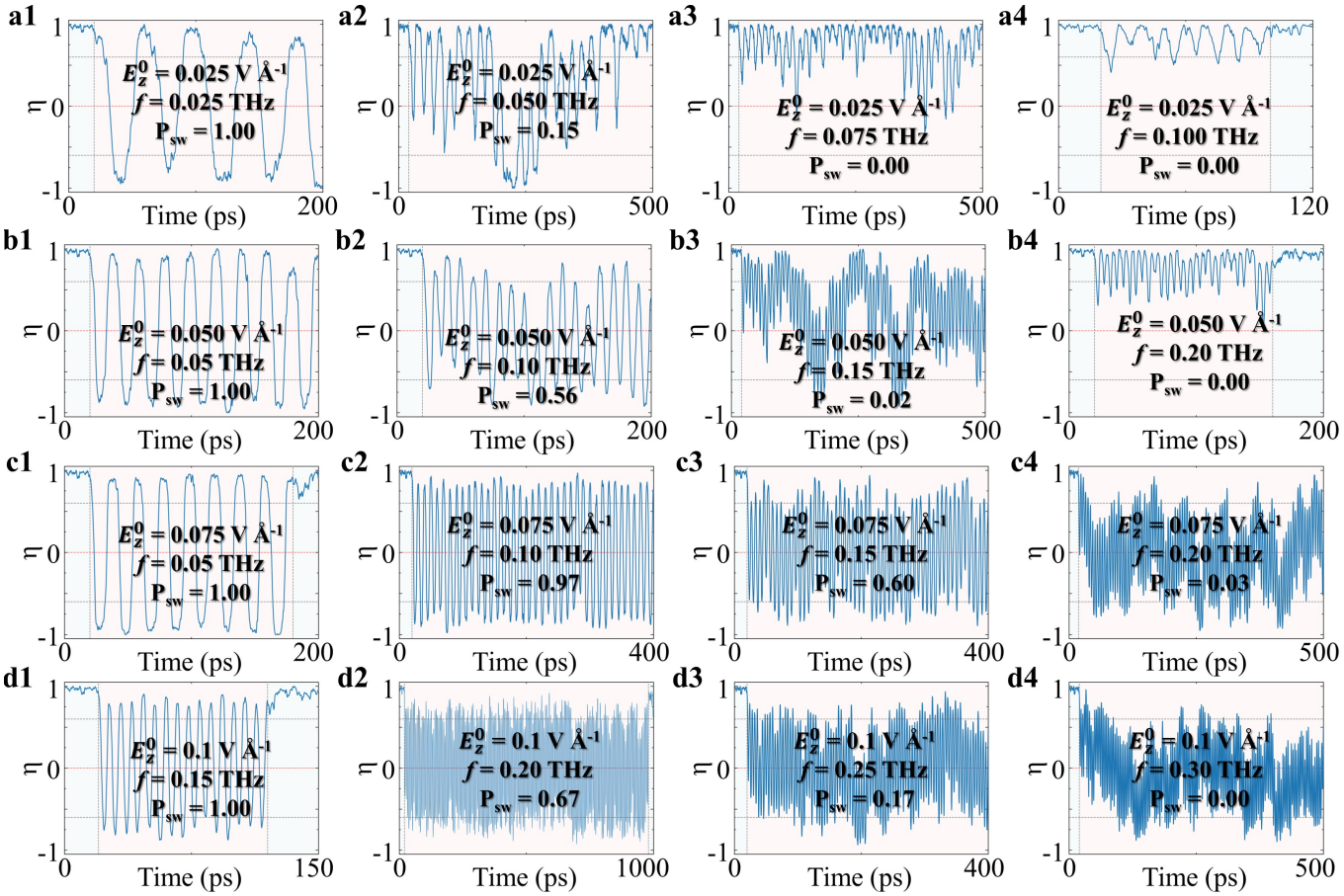
The numerical switching probabilities at 200, 250, and 300 K are summarized in Supplementary Tables 5, 6, and 7, respectively. The values shown in Supplementary Figs. 13–15 were evaluated using all complete cycles available in each trajectory, although shorter time windows are displayed for clarity.



Supplementary Figure 13. **Oscillating-field-driven Ag-sublattice switching at 200 K.** Ag-sublattice switching driven by an oscillating out-of-plane field at 200 K without an in-plane probe field. Rows **a**–**c** correspond to amplitudes $E_z^0 = 0.050$, 0.075, and 0.100 V Å^{-1}, respectively. Frequencies and switching probabilities P_{sw} are indicated in each panel. Probabilities are evaluated over all complete field cycles, while the displayed intervals resolve representative switching dynamics.



Supplementary Figure 14. **Oscillating-field-driven Ag-sublattice switching at 250 K.** Ag-sublattice switching at 250 K without an in-plane probe field. Rows **a**–**d** correspond to amplitudes E_z^0 = 0.025, 0.050, 0.075, and 0.100 V Å^{-1}, respectively. Frequencies and complete-cycle switching probabilities are indicated in each panel, using the same definition as in Supplementary Fig. 13.



Supplementary Figure 15. **Oscillating-field-driven Ag-sublattice switching at 300 K.** Ag-sublattice switching at 300 K without an in-plane probe field. Rows **a**–**d** correspond to amplitudes E_z^0 = 0.025, 0.050, 0.075, and 0.100 V Å^{-1}, respectively. Frequencies and complete-cycle switching probabilities are indicated in each panel, using the same definition as in Supplementary Fig. 13.

Supplementary Table 5. Individual-trajectory switching probabilities at 200 K with $E_x = 0$.

E_z^0 (V Å^{-1})	f (THz)	P_{sw}	E_z^0 (V Å^{-1})	f (THz)	P_{sw}
0.030	0.015	0.250	0.100	0.050	1.000
	0.025	0.000		0.100	1.000
	0.050	0.000		0.150	0.733
	0.075	0.000		0.200	0.204
	0.100	0.000		0.300	0.000
0.050	0.050	0.902		0.400	0.000
	0.075	0.315		0.500	0.000
	0.100	0.000			
	0.200	0.000			
	0.300	0.000			
0.075	0.100	0.800			
	0.150	0.071			
	0.200	0.000			
	0.400	0.000			

Supplementary Table 6. Individual-trajectory switching probabilities at 250 K with $E_x = 0$.

E_z^0 (V Å^{-1})	f (THz)	P_{sw}	E_z^0 (V Å^{-1})	f (THz)	P_{sw}
0.025	0.015	0.714	0.100	0.100	1.000
	0.020	0.737		0.150	0.933
	0.025	0.542		0.200	0.503
	0.040	0.000		0.300	0.000
	0.050	0.000		0.400	0.000
	0.060	0.000		0.500	0.000
0.050	0.050	1.000		0.600	0.000
	0.075	0.753		0.700	0.000
	0.100	0.143		0.800	0.000
	0.150	0.000		0.900	0.000
	0.200	0.000			
	0.250	0.000			
	0.300	0.000			
0.075	0.100	1.000			
	0.150	0.361			
	0.200	0.031			
	0.300	0.000			

Supplementary Table 7. Individual-trajectory switching probabilities at 300 K with $E_x = 0$.

E_z^0 (V Å^{-1})	f (THz)	P_{sw}	E_z^0 (V Å^{-1})	f (THz)	P_{sw}
0.025	0.025	1.000	0.100	0.050	1.000
	0.050	0.152		0.075	1.000
	0.075	0.000		0.100	1.000
	0.100	0.000		0.150	1.000
	0.500	0.000		0.200	0.667
	1.000	0.000		0.250	0.168
	5.000	0.000		0.300	0.003
0.030	0.030	1.000		0.400	0.000
	0.040	1.000		0.500	0.000
	0.050	0.429		0.600	0.000
	0.100	0.000		0.700	0.000
	0.200	0.000		0.800	0.000
	0.300	0.000		0.900	0.000
0.050	0.050	1.000		1.000	0.000
	0.100	0.556		5.000	0.000
	0.150	0.018			
	0.200	0.000			
	0.250	0.000			
	0.300	0.000			
	0.500	0.000			
	1.000	0.000			
	5.000	0.000			
0.075	0.050	1.000			
	0.100	0.974			
	0.150	0.596			
	0.200	0.029			
	0.300	0.000			
	0.400	0.000			
	0.500	0.000			
	0.600	0.000			

8.2. Estimation of the characteristic switching timescale

For each temperature and out-of-plane field amplitude, the characteristic switching frequency f_{sw} was obtained by linear interpolation between the two neighboring sampled frequencies, f_{lower} and f_{upper}, with measured P_{sw} above and below 0.5, respectively. The characteristic switching timescale was then defined as $\tau_{\mathrm{sw}} = 1/(2f_{\mathrm{sw}})$. This definition ensures $f_{\mathrm{lower}} \leq f_{\mathrm{sw}} \leq f_{\mathrm{upper}}$. The neighboring sampled frequencies therefore define a half-period range of $[1/(2f_{\mathrm{upper}}),\ 1/(2f_{\mathrm{lower}})]$, which indicates the local resolution of the discrete frequency scan rather than a statistical confidence interval. The 200 and 250 K values were obtained from trajectories with $E_x = 0$, whereas those at 300 K include trajectories with both $E_x = 0$ and $E_x = +0.0025$ V Å^{-1}. For example, at $T = 300$ K and $E_z^0 = 0.030$ V Å^{-1}, the interpolation yields $f_{\mathrm{sw}} \simeq 0.055$ THz and thus $\tau_{\mathrm{sw}} \simeq 9.1$ ps. The resulting switching frequencies and timescales are summarized in Supplementary Table 8.

Supplementary Table 8. Characteristic switching frequencies and timescales. f_{lower} and f_{upper} denote the neighboring sampled frequencies with measured P_{sw} above and below 0.5, respectively. f_{sw} was obtained by linear interpolation within this interval.

T (K)	E_z^0 (V Å^{-1})	f_{lower} (THz)	f_{upper} (THz)	f_{sw} (THz)	τ_{sw} (ps)
200	0.050	0.050	0.075	0.067	7.448
	0.075	0.100	0.150	0.121	4.146
	0.100	0.150	0.200	0.172	2.907
250	0.025	0.025	0.040	0.026	19.118
	0.050	0.075	0.100	0.085	5.856
	0.075	0.100	0.150	0.139	3.594
	0.100	0.200	0.300	0.201	2.493
300	0.025	0.025	0.050	0.038	13.261
	0.030	0.050	0.060	0.055	9.124
	0.050	0.100	0.150	0.105	4.755
	0.075	0.150	0.200	0.159	3.155
	0.100	0.200	0.250	0.216	2.315

SUPPLEMENTARY REFERENCES

[1] G. Kresse and J. Furthmüller, Efficient iterative schemes for ab initio total-energy calculations using a plane-wave basis set, Phys. Rev. B **54**, 11169 (1996).

[2] P. E. Blöchl, Projector augmented-wave method, Phys. Rev. B **50**, 17953 (1994).

[3] J. P. Perdew, K. Burke, and M. Ernzerhof, Generalized gradient approximation made simple, Phys. Rev. Lett. **77**, 3865 (1996).

[4] S. Baroni, S. de Gironcoli, A. Dal Corso, and P. Giannozzi, Phonons and related crystal properties from density-functional perturbation theory, Rev. Mod. Phys. **73**, 515 (2001).

[5] S. Grimme, J. Antony, S. Ehrlich, and H. Krieg, A consistent and accurate ab initio parametrization of density functional dispersion correction DFT-D for the 94 elements H-Pu, J. Chem. Phys. **132**, 154104 (2010).

[6] S. Nosé, A unified formulation of the constant temperature molecular dynamics methods, J. Chem. Phys. **81**, 511 (1984).

[7] A. Hjorth Larsen, J. Jørgen Mortensen, J. Blomqvist, I. E. Castelli, R. Christensen, M. Duak, J. Friis, M. N. Groves, B. Hammer, C. Hargus, E. D. Hermes, P. C. Jennings, P. Bjerre Jensen, J. Kermode, J. R. Kitchin, E. Leonhard Kolsbjerg, J. Kubal, K. Kaasbjerg, S. Lysgaard, J. Bergmann Maronsson, T. Maxson, T. Olsen, L. Pastewka, A. Peterson, C. Rostgaard, J. Schiøtz, O. Schütt, M. Strange, K. S. Thygesen, T. Vegge, L. Vilhelmsen, M. Walter, Z. Zeng, and K. W. Jacobsen, The atomic simulation environmenta python library for working with atoms, J. Phys. Condens. Matter **29**, 273002 (2017).

[8] J.-W. Li, S. Meng, X. Shi, J. Zhang, and W.-H. Fang, A unified graph neural network framework for non-equilibrium carrier and lattice dynamics driven by electric fields (2026).

[9] J. Wang, J. Ding, O. Delaire, and G. Arya, Atomistic mechanisms underlying non-arrhenius ion transport in superionic conductor $AgCrSe_2$, ACS Appl. Energy Mater. **4**, 7157 (2021).

[10] J. Yang, L. Xie, M. Hu, Y. Qi, J. Li, B. Jia, J. Feng, Z. Chen, M. Bosman, D. Xiang, and J. He, Tracking ultrafast ion diffusion dynamics in $AgCrSe_2$ superionic conductor, Phys. Rev. X **16**, 021024 (2026).